

Marangoni-driven pattern transition and the formation of ridges and hills in surfactant-covered parametric surface waves

Debashis Panda,¹ Lyes Kahouadji,¹ Laurette S. Tuckerman,² Seungwon Shin,³ Jalel Chergui,⁴ Damir Juric,^{4,5} and Omar K Matar^{6,*}

¹Imperial College London, South Kensington Campus, London SW7 2AZ, United Kingdom

²Physique et Mécanique des Milieux Hétérogènes, CNRS, ESPCI Paris, Université PSL, Sorbonne Université, Université de Paris, 75005 Paris, France

³Hongik University, Seoul 04066, Republic of Korea

⁴Laboratoire Interdisciplinaire des Sciences du Numérique (LISN), CNRS, Université de Paris Saclay, 91400 Orsay, France

⁵University of Cambridge, Centre for Mathematical Sciences, Wilberforce Road, Cambridge CB3 0WA, United Kingdom

⁶Imperial College London, South Kensington Campus, London SW7 2AZ, United Kingdom

(Dated: December 30, 2024)

Nonlinear surface waves are excited via a parametric oscillation of a surfactant-covered interface. Increasing the relative magnitude of the surfactant-induced Marangoni stresses results in a pattern transition from squares (observed for surfactant-free interfaces) to asymmetric squares, weakly wavy stripes, and ridges and hills. These hills are a consequence of the bi-directional Marangoni stresses at the neck of the ridges. The mechanisms underlying the pattern transitions and the formation of exotic ridges and hills are discussed in this Letter.

Faraday [1] noticed that the vertical vibration of a fluid layer produces surface waves oscillating at half the driving frequency. Crossing a threshold amplitude, these *Faraday surface waves* usually organize into patterns like squares, hexagons, stripes, quasipatterns, and superlattices. Complications arise from factors such as contact line dissipation [2], multi-frequency forcing [3], and surface contamination [4]. Surfactant-covered Faraday waves have been studied to assess the damping rates of surface waves [5–7] due to the influence of Marangoni stresses [4, 8]. However, these studies are limited to linearised one- or two-dimensional models, with some being carried out using lubrication theory, lacking three-dimensional studies of strongly nonlinear Marangoni effects on pattern formation in Faraday waves.

In this Letter, we report the results of simulations of the three-dimensional surfactant-covered Faraday waves; we focus on the influence of Marangoni effects on the surface wave patterns. Our study reveals that increasing the relative importance of Marangoni stresses leads to transitions from square patterns to asymmetric squares, weakly wavy stripes, and ridges and hills. These ridges and hills are new features that occur at higher Marangoni number (or B as defined in this Letter). Ridges are found to rise non-uniformly and fall by forming a hill. Our direct numerical simulations help uncover the rich physics of the dynamics of these newly observed ridges and hills.

Our computational domain is a laterally-periodic box of area $\tilde{\lambda}_c \times \tilde{\lambda}_c$ and height \tilde{H} , where $\tilde{\lambda}_c$ is the critical wavelength. A thin film of a water-glycerine mixture (of density $\tilde{\rho}_w = 1000 \text{ kg/m}^3$, viscosity $\tilde{\mu}_w = 0.025 \text{ kg/m s}$) of depth $\tilde{h} = 1 \text{ mm}$ is considered with air as the background fluid. The interface (of surface tension $\tilde{\sigma} = 70 \text{ mN/m}$) is vibrated at an angular frequency $\omega = 200\pi \text{ rad/s}$ and acceleration amplitude \tilde{A} . We assume that a layer of insoluble surfactant monomers (of concentration $\tilde{\Gamma}$) covers the interface

such that the number of moles of monomers on the surface is conserved. The surfactant-dependent surface tension is parameterised by the Langmuir-Szyszkowski equation of state, $\tilde{\sigma}(\tilde{\Gamma})/\tilde{\sigma}_0 = 1 + \beta_s \ln(1 - \tilde{\Gamma}/\tilde{\Gamma}_\infty)$, where $\tilde{\Gamma}_\infty$ is the maximum packing concentration and β_s is the elasticity parameter reflecting the effectiveness of the surfactant in lowering $\tilde{\sigma}$.

We initialize our simulations with a plane interface and uniformly distributed surfactant coverage $\tilde{\Gamma}_0$. The interfacial dynamics are coupled to a surfactant transport equation that accounts for inertia, viscosity, gravity, capillarity, Marangoni stresses, surface diffusion, and parametric forcing [10]. Non-dimensionalization of the equations is carried out, in which \tilde{h} , $1/\omega$, and $\tilde{\Gamma}_\infty$ are taken as the characteristic length, time, and concentration scales, leading to six dimensionless numbers. We set these and their values to be Reynolds $Re \equiv \tilde{\rho}_w \tilde{h}^2 \omega / \tilde{\mu}_w = 25.3$, Weber $We \equiv \tilde{\rho}_w \tilde{h}^3 \omega^2 / \tilde{\sigma}_0 = 18.37$, Péclet, $Pe \equiv \tilde{h}^2 \omega / \mathcal{D} = 2.5 \times 10^5$, and Froude $Fr \equiv \omega \sqrt{\tilde{h}/g} = 6.34$ numbers. Rather than the usual Marangoni number, $Ma = \beta_s / We$, we introduce $B \equiv (\tilde{\sigma}_0 - \tilde{\sigma}(\tilde{\Gamma}_0)) / (\tilde{\mu}_w \tilde{h} \omega)$, which is the ratio of vibratory inertial and Marangoni timescales, to quantify the combined effects of β_s and $\tilde{\Gamma}_0$; B is varied systematically to assess the emergent pattern transitions at the acceleration amplitude obtained by $F = \tilde{A}/g$. Detailed descriptions of the formulation, scaling, and numerical method [10] are presented in Section A of the supplemental material [9].

After a transient phase, Faraday waves appear, which correspond to subharmonic waves whose amplitude is steady and whose response period T is twice that of the forcing period. We set $t = 0$ to be an instant within the steady-amplitude Faraday-wave regime. Hereafter, we discuss our results in terms of dimensionless variables (with the tilde suppressed). The dimensionless critical wavelength λ_c and acceleration amplitude F_c for a clean interface are 5.30 and 12.34, respectively. We studied the effect of varying B on the threshold

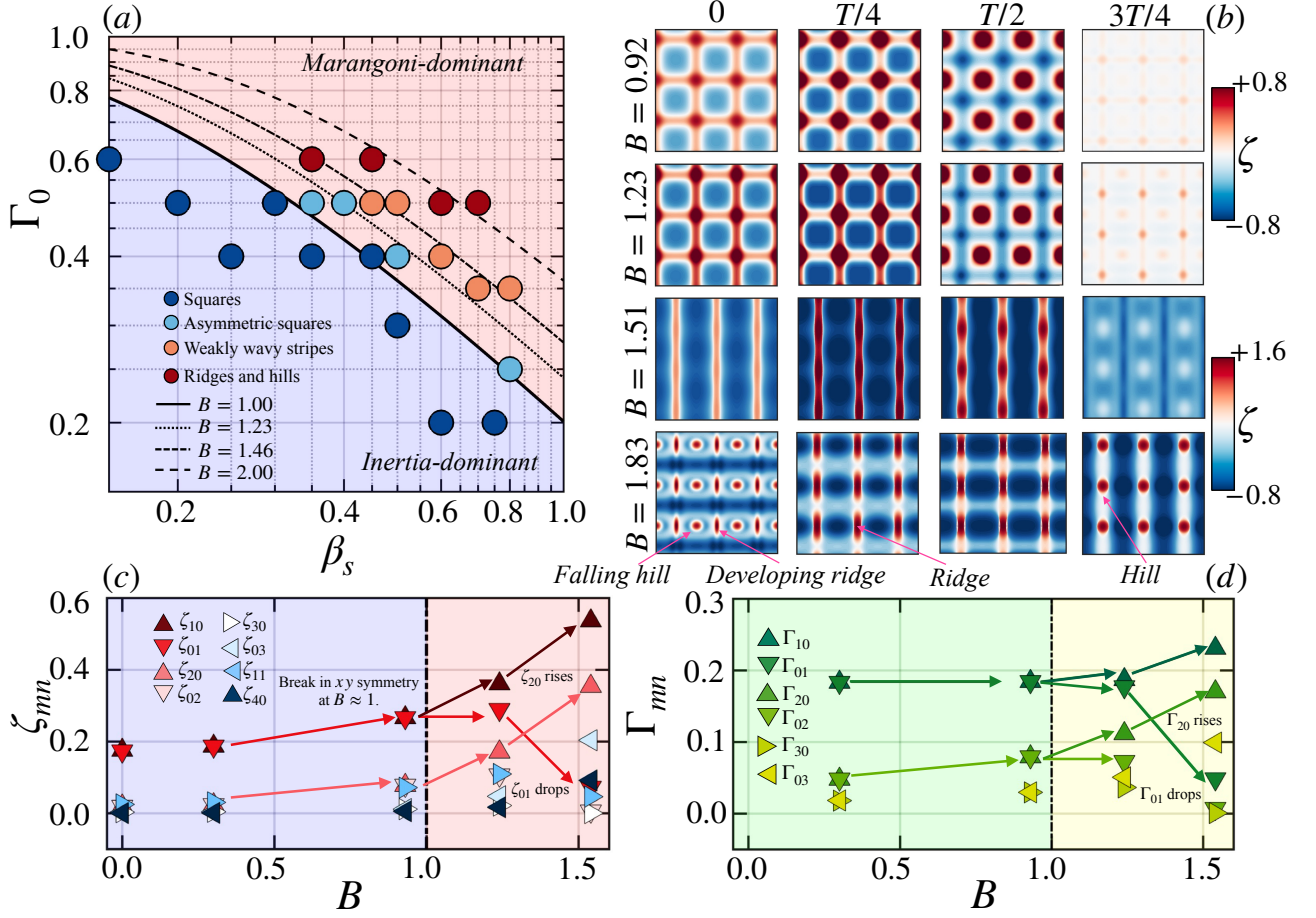


FIG. 1. (a) Phase diagram in the $\beta_s - \Gamma_0$ parameter plane showing the inertia-dominated (violet) and Marangoni-dominated (pink) regions. The solid, dotted, dot-dashed, and dashed lines correspond to the $B = 1, 1.23, 1.46, 2$ contours, respectively. The four typical patterns are squares, asymmetric squares, weakly wavy stripes, and ridges and hills. The phase boundaries are accurate to within $\Delta B = \pm 0.1$. The corresponding values of B and F_c^N are reported in table II of the supplemental material [9]. (b) Spatiotemporal evolution of the surface deflection ζ over one time period is shown from left to right; squares ($B = 0.92$), asymmetric squares ($B = 1.23$), weakly wavy stripes ($B = 1.51$), and ridges and hills ($B = 1.83$) are shown from top to bottom rows, respectively. (c,d) ζ_{mn} and Γ_{mn} , the maximal magnitudes over time of the ζ and Γ Fourier coefficients, respectively, as a function of B .

acceleration F_c^N with the details provided in Section B of the supplemental material [9]. Our results show that increasing B stabilises the interface, as observed in previous studies [4, 5]. The computations for assessing the influence of B on the interfacial dynamics in the nonlinear regime are then carried out for $F = 1.1F_c^N$ for which square patterns are observed in the surfactant-free case.

As shown in Fig. 1(a), for $B < 1$ (dark blue dots, purple region), the interface exhibits square symmetry. In a narrow band of $1 \leq B \leq 1.23$ (light blue dots), the vertical and horizontal directions differ slightly; we refer to these patterns as *asymmetric squares*. Within $1.23 \leq B \leq 1.46$ (orange dots), the asymmetric square pattern undergoes a transition to *weakly wavy stripes*. Ridges (ellipses whose major axes are in the y -direction) appear very faintly as dots for $B = 1.23, t = 3T/4$, and more prominently on the wavy stripes for $B = 1.51$. For $B = 1.83, t = 0$, one can also see circular hills between each set of ridges. The hills are the continuation

of the ridges formed in the previous half-period. One such instance is shown at $t = 3T/4$, where the ridges have disappeared but the hills are present. We explore below the role of Marangoni stresses in the formation of these patterns.

To quantify the patterns, we evaluate the spatial Fourier spectra for the surface height, ζ , and surfactant concentration, Γ , defining $\hat{\zeta}_{mn}(t)$ and $\hat{\Gamma}_{mn}(t)$ to be the Fourier coefficients associated with the (x, y) wavevector \mathbf{k}_{mn} . We then set $\zeta_{mn} \equiv \max_{[t, t+T]} |\hat{\zeta}_{mn}(t)|$ and $\Gamma_{mn} \equiv \max_{[t, t+T]} |\hat{\Gamma}_{mn}(t)|$. Figures 1(c,d) present an overview of the spatial Fourier spectra of ζ and Γ as a function of B in the range $B \in [0, 1.51]$. At higher B , ridges and hills emerge, where steep spatial gradients and many higher spatial harmonics appear.

For $B < 1$, the square pattern is characterized by comparable amplitudes of ζ_{10} and ζ_{01} , as shown in Fig. 1(c). For $B < 0.5$, where Marangoni effects are weak, the ζ_{mn} modes have magnitudes similar to those associated with the clean case corresponding to $B = 0$, consistent with previous find-

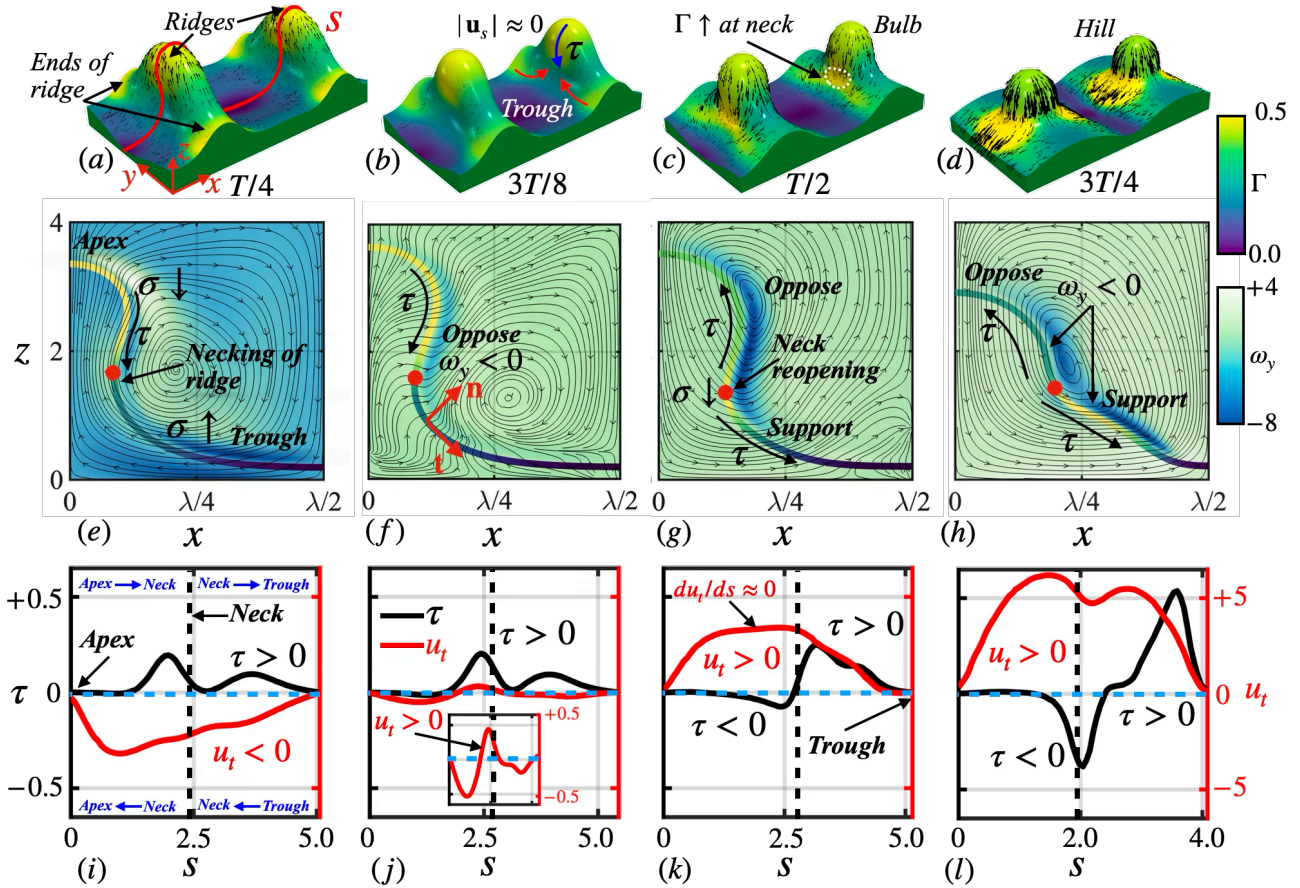


FIG. 2. (a)-(d) Three-dimensional visualization of the surface. (a) Rise of ridges and necking process at $t = T/4$ and (b) maximum rise of the ridge at $t = 3T/8$. (c) Prominent hill on the ridge at $t = T/2$. (d) Falling hill at $t = 3T/4$. (e-h) Two-dimensional projections on $x-z$ slice containing interface curve s (indicated in (a)) for $t = T/4, 3T/8, T/2$, and $3T/4$, respectively. A half-wavelength (ridge to trough) is shown. Color-coding of the plane indicates y -vorticity ω_y , while streamlines show flow in $x-z$ plane. The interface curve s is colored according to the surfactant concentration. Red dots indicate the point of maximum curvature. (i-l) Tangential (see (f)) Marangoni stress and velocity along s at $t = T/4, 3T/8, T/2$, and $3T/4$ shown as black and red curves, respectively. When the sign of one of these quantities is positive (negative), its direction points rightwards (leftwards) from the apex (trough) through the neck to the trough (apex) of the ridge, as indicated at the top (bottom) of Fig. 2(i). The vertical dashed line indicates the necking region, shown as the red dot in the corresponding $x-z$ projection. The length of s decreases from about 5 at $t = T/4, 3T/8, T/2$ to about 4 at $t = 3T/4$, as can be seen in the curves in (e-h).

ings [11, 12]. For $B > 1$, Marangoni-driven stresses dominate over inertial effects. The square symmetry is broken, and by $B = 1.23$, ζ_{10} surpasses ζ_{01} , with an increase in higher-order modes, such as the ζ_{20} mode. As B increases further, strong x -dependent modes emerge, leading to a transition from asymmetric squares to stripes (see Fig. 1(c)).

A parallel change occurs in the Γ -spectrum. For $B < 1$, the surfactant is advected without being significantly hindered by Marangoni stresses, aligning the Γ -spectrum with the ζ -spectrum, where Γ_{10} and Γ_{01} dominate (see Fig. 1(d)). For $B > 1$, Γ_{10} begins to surpass Γ_{01} . Thus, $B \approx 1$ is a pivotal point in the dynamics, at which there is an equilibrium between the opposing mechanisms of advection-driven surfactant inhomogeneity and Marangoni-driven homogeneity.

We now turn to the formation of hills and ridges on the interface. Figures 2(a-d) illustrate the evolution of a small portion of the interface, color-coded by surfactant concentration.

During the first half-cycle, the ridges rise, and the fluid and surfactant flow up from the troughs, advecting the surfactant to the apex of the ridge. Figures 2(e-h) show two-dimensional projections containing arc s , as indicated in Fig. 2(a). As the surfactant is advected towards the apex, a Γ -deficit (higher σ) is created at the trough.

The capillary force resulting from the Γ -deficit leads to the emergence of a bulb on the ridge, surrounded by a narrow region of negative curvature, which we call a *neck*, and which is highlighted by a red spot on the interface in Figs. 2(e-h); Γ accumulates at the ends of the ridge as shown in Figs. 2(a,b). Marangoni stresses along s counteract the Γ -inhomogeneity caused by the surface advection. This is shown in Fig. 2(i), where $\tau > 0$ and $u_t < 0$ along the arc s . We call this a *barrier*. This barrier rigidifies the surface during the first half-cycle, leading to $|\mathbf{u}_s| \approx 0$ at $t = 3T/8$, as shown in Fig. 2(b).

The negative vorticity along the surface in Fig. 2(f) indi-

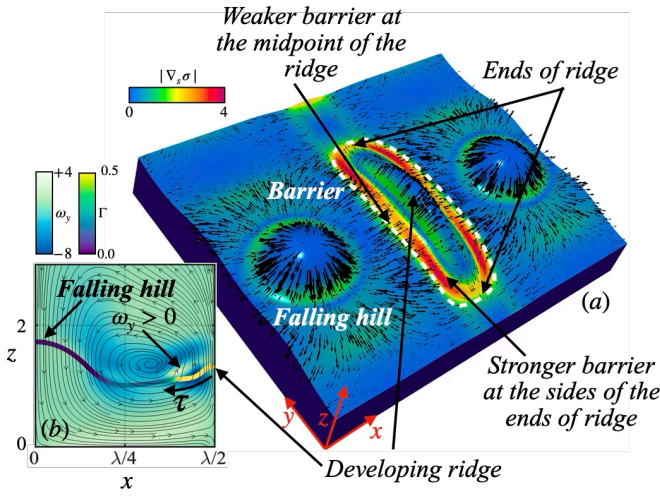


FIG. 3. Marangoni-influenced ridge formation: (a) $x-z$ projection containing s , as defined in Fig. 2, at $t = T$; the color-coding used here is that of Fig. 2. (b) Three-dimensional visualization of the interface color-coded by the magnitude of Marangoni stresses $|\nabla_s \sigma|$, indicating the barriers around the rising ridge.

ates that τ opposes the surface advection. Due to this barrier, a backflow develops on the surface from the apex towards the neck, as indicated by $u_t > 0$ in the inset of Fig. 2(j). This drives surfactants from the apex towards the neck. Simultaneously, the accumulated surfactant at the ends of the ridge flows towards the neck due to a similar mechanism, as illustrated by the red arrows in Fig. 2(b). During this process, the midpoint of the ridge rises to form a bulb; see Fig. 2(c). By $t = T/2$, Γ is maximal (so σ is minimal) at the neck.

The accumulated surfactant causes Marangoni stresses, with distinct peaks of $\tau > 0$ and $\tau < 0$ across the neck (Fig. 2(k)). The barrier is now formed at the neck (shown as a white dotted region in Fig. 2(c)) where these stresses in the region between the apex and the neck begin to oppose the flow reversal at half-cycle. Meanwhile, surface tension decreases at the neck. As a result, the neck begins to reopen (see the streamlines in fig. 2(g)) as is commonly observed in surfactant-laden neck reopening phenomena, discussed in detail in [12, 13].

In the next half-cycle ($t \geq T/2$), the ridge begins to fall. However, the opposing Marangoni stress between the neck and the apex ($\tau < 0$ in Fig. 2(k)) slows the collapse of this region. This slower descent of u_t ($du_t/ds \approx 0$) leads to the formation of the hill on the ridge. Meanwhile, at $t = 3T/4$, the region between the neck and the trough continues to fall more quickly than the hill. This accelerated fall is driven by the surfactant gradients towards the trough ($\tau > 0$ as shown in Fig. 2(l)) which, instead of opposing the bulk flow as before, now begin to support it due to $u_t > 0$. The presence of two high-vorticity regions (blue zones) along the interface in Fig. 2(h) is an effect of the two distinct roles of Marangoni stresses at the neck. As a consequence, new ridges develop while the hills of the previous cycle are still present, as seen in Fig. 1 at $t = 0$, $B = 1.83$.

Figure 3 further elucidates the mechanism of ridge formation. The surfactant accumulates on the developing ridge due to a combination of Marangoni-driven surface flow from the neck to the trough ($\tau > 0$ in Fig. 2(h,l)) as previously discussed, and advection through bulk flow in the second half-cycle leading to strong surface compression at the ridge. This accumulation (see Γ -surplus region highlighted in Fig. 3(a)) generates a Marangoni stress, directed from the newly developed ridge toward the falling hill (as highlighted by the arrow indicating the direction of τ in Fig. 3(a)). The magnitude of the Marangoni stress, $|\nabla_s \sigma|$, is shown in Fig. 3(b). This high-stress region, which surrounds the developing ridge, highlights the strength of the barrier to ridge formation. Close inspection of this region reveals that the barrier is weaker at the midpoint of the ridge, allowing stronger inward-directed surface flow to this region (viz. the velocity glyphs in Fig. 3(b)). This, in turn, leads to a higher elevation at the midpoint of the ridge than at its ends, as shown in Fig. 3(b).

The study highlights the role of Marangoni stresses in Faraday wave pattern transitions. Using a dimensionless parameter B to compare the Marangoni and inertial timescales, we found that for $B \approx 1$, the square patterns are succeeded by asymmetric squares and then by weakly wavy stripes as B is further increased. The novel finding highlighted here is that for higher B values, ridges and hills appear. Due to strong Marangoni flow during a cycle of forcing, surfactant- and vibration-induced surface flows compete, giving rise to a Marangoni-driven barrier, which is the cause of these interesting ridges and hills.

We thank EPSRC for support through the PREMIERE (EP/T000414/1) programme grant, and the ANTENNA Prosperity Partnership (EP/V056891/1). D.J. and J.C. thank the Institut du Developpement et des Ressources en Informatique Scientifique of the CNRS, coordinated by GENCI (Grand Equipement National de Calcul Intensif) grant 2024 A0162B06721. D.P. thanks Imperial for a President PhD scholarship, and Prof. Cédric Beaume for fruitful discussions.

* o.matar@imperial.ac.uk

- [1] M. Faraday, On the forms and states of fluids on vibrating elastic surfaces, *Phil. Trans. Roy. Soc* **52**, 319 (1831).
- [2] H. Alarcón, M. Herrera-Muñoz, N. Périnet, N. Mujica, P. Gutiérrez, and L. Gordillo, Faraday-wave contact-line shear gradient induces streaming and tracer self-organization: From vortical to hedgehoglike patterns, *Phys. Rev. Lett.* **125**, 254505 (2020).
- [3] W. S. Edwards and S. Fauve, Patterns and quasi-patterns in the Faraday experiment, *J. Fluid Mech.* **278**, 123 (1994).
- [4] S. Ubal, M. D. Giavedoni, and F. A. Saita, Elastic effects of an insoluble surfactant on the onset of two-dimensional Faraday waves: a numerical experiment, *J. Fluid Mech.* **524**, 305 (2005).
- [5] D. M. Henderson, Effects of surfactants on Faraday-wave dynamics, *J. Fluid Mech.* **365**, 89 (1998).
- [6] S. Kumar and O. K. Matar, Parametrically driven surface waves

- in surfactant-covered liquids, *Proc. Roy. Soc. A* **458**, 2815 (2002).
- [7] S. Kumar and O. K. Matar, On the Faraday instability in a surfactant-covered liquid, *Phys. Fluids* **16**, 39 (2004).
- [8] S. Ubal, M. D. Giavedoni, and F. A. Saita, The formation of Faraday waves on a liquid covered with an insoluble surfactant: Influence of the surface equation of state, *Lat. Am. Appl. Res.* **35**, 59 (2005).
- [9] (2024), see supplemental material which includes problem set-up, scaling, Floquet analysis, and numerical method validation.
- [10] S. Shin, J. Chergui, and D. Juric, A solver for massively parallel direct numerical simulation of three-dimensional multiphase flows, *J. Mech. Sci. Tech.* **31**, 1739 (2017).
- [11] C. R. Constante-Amores, L. Kahouadji, A. Batchvarov, S. Shin, J. Chergui, D. Juric, and O. K. Matar, Dynamics of retracting surfactant-laden ligaments at intermediate Ohnesorge number, *Physical Review Fluids* **5**, 084007 (2020).
- [12] C. R. Constante-Amores, J. Chergui, S. Shin, D. Juric, J. Castrejón-Pita, and A. A. Castrejón-Pita, Role of surfactant-induced Marangoni stresses in retracting liquid sheets, *J. Fluid Mech.* **949**, A32 (2022).
- [13] C. Constante-Amores, A. Batchvarov, L. Kahouadji, S. Shin, J. Chergui, and O. Matar, Role of surfactant-induced Marangoni stresses in drop-interface coalescence, *J. Fluid Mech.* **925**, A15 (2021).

Supplemental material: Marangoni-driven pattern transition and the formation of ridges and hills in surfactant-covered parametric surface waves

Debashis Panda,¹ Lyes Kahouadji,¹ Laurette S. Tuckerman,² Seungwon Shin,³ Jalel Chergui,⁴ Damir Juric,^{4,5} and Omar K Matar^{1,*}

¹*Department of Chemical Engineering, Imperial College London, South Kensington Campus, London SW7 2AZ, United Kingdom*

²*Physique et Mécanique des Milieux Hétérogènes, CNRS, ESPCI Paris, Université PSL, Sorbonne Université, Université de Paris, 75005 Paris, France*

³*Department of Mechanical and System Design Engineering, Hongik University, Seoul 04066, Republic of Korea*

⁴*Université Paris Saclay, Centre National de la Recherche Scientifique (CNRS), Laboratoire Interdisciplinaire des Sciences du Numérique (LISN), 91400 Orsay, France*

⁵*Department of Applied Mathematics and Theoretical Physics, University of Cambridge, Centre for Mathematical Sciences, Wilberforce Road, Cambridge CB3 0WA, United Kingdom*

(Dated: December 30, 2024)

A. PROBLEM SET-UP, NON-DIMENSIONALIZATION AND CHOICE OF PARAMETERS

Our computational domain is a cuboid of area $\lambda_c \times \lambda_c$ and height $H = 5$, where λ_c is the critical wavelength for our configuration. Figure 1(a) shows this domain, which contains a layer of heavy fluid overlaid by light fluid. No-penetration and no-slip boundary conditions are applied at the bottom and top of the domain and periodic boundaries on the sides (see figure 1(a)). The interface is initially perturbed with a sinusoidal wave of wavevector $|\mathbf{k}| = k_c \mathbf{e}_x$. A resolution of $|\Delta x| = |\Delta y| = \lambda_c/44$ was found to be necessary to capture the Faraday wave dynamics in [1–3]. We choose a finer resolution of $\lambda_c/128$ to capture the coupling with the surfactant dynamics.

We used a hybrid level-set/front-tracking method to track the liquid-gas interface. We choose a simulation set-up and hydrodynamic parameters similar to those reported in [4]: the lower heavy fluid is a water-glycerine mixture of depth $\tilde{h} = 1$ mm with density $\tilde{\rho}_w = 1000$ kg/m³ and dynamic viscosity $\tilde{\mu}_w = 0.025$ kg/ms. In contrast to [4], rather than neglecting the effects of the upper fluid, we consider a layer of air of height 4 mm, density $\tilde{\rho}_a = 1.206$ kg/m³ and dynamic viscosity $\tilde{\mu}_a = 1.82 \times 10^{-5}$ kg/ms. Because the ratio of the density of the lighter to that of the lower fluid is only 10^{-3} and the capillary length $l_c = \sqrt{\tilde{\sigma}_0/\Delta\tilde{\rho}g} = 2.67$ mm is less than the height 4mm of the lighter fluid, the lighter fluid has little effect on the Faraday instability and we can compare our results to those of [4].

The surface tension of the liquid-gas surfactant-free interface is $\tilde{\sigma}_0 = 70 \times 10^{-3}$ kg/s². The frequency of the external vibration is 100 Hz, leading to angular frequency $\omega = 2\pi 100$ rad/s.

We consider an insoluble surfactant that is present only on the interface. This means that the timescale of surfactant desorption from the interface into the bulk is larger than the vibratory timescale. The saturated surfactant concentration at the critical micelle concentration is $\tilde{\Gamma}_\infty \sim \mathcal{O}(10^{-6})$; the range of surfactant elasticity parameter β_s (whose definition is discussed in the following section) is $0.1 < \beta_s < 0.9$. The diffusivity for the surfactant \mathcal{D} is set to 2.5×10^{-9} m²/s to align with the work of [4, 6]. Unless otherwise specified, we set the initial surfactant coverage to $\tilde{\Gamma}_0 = 0.5\tilde{\Gamma}_\infty$.

We list the major timescales in the problem: (i) the capillary timescale $\Delta\tilde{t}_c = (\tilde{\rho}_w \tilde{h}^3 / \tilde{\sigma}_0)^{1/2}$ of natural capillary oscillations of the perturbed planar interface; (ii) the imposed vibrational timescale $\Delta\tilde{t}_i = 1/\omega$; and (iii) the Marangoni timescale $\Delta\tilde{t}_m = \tilde{\mu}_w \tilde{h} / (\tilde{\sigma}_0 - \tilde{\sigma}(\tilde{\Gamma}_0))$, where $\tilde{\sigma}$ denotes the surface tension of a surfactant-laden interface, which quantifies the surfactant dynamics on the interface. Our choice of parameters leads to $\Delta\tilde{t}_c \sim \mathcal{O}(10^{-3})$, $\Delta\tilde{t}_i \sim \mathcal{O}(10^{-3})$, and $\Delta\tilde{t}_m \sim \mathcal{O}(10^{-4} - 10^{-3})$. This choice ensures that we observe a competition between the vibrational, capillary, and Marangoni effects.

We choose the height of the liquid \tilde{h} as the length scale, the inverse angular frequency $1/\omega$ as the timescale, and $\omega^2 \tilde{\rho}_w \tilde{h}^2$ as the pressure scale. Finally, the interfacial concentration $\tilde{\Gamma}$ is scaled by the saturated interfacial concentration $\tilde{\Gamma}_\infty$, yielding:

$$\mathbf{x} = \frac{\tilde{\mathbf{x}}}{\tilde{h}}, \quad t = \tilde{t}\omega, \quad \mathbf{u} = \frac{\tilde{\mathbf{u}}}{\omega\tilde{h}}, \quad p = \frac{\tilde{p}}{\tilde{\rho}_w \tilde{h}^2 \omega^2}, \quad \sigma = \frac{\tilde{\sigma}}{\tilde{\sigma}_0}, \quad \Gamma = \frac{\tilde{\Gamma}}{\tilde{\Gamma}_\infty}, \quad (1)$$

The dimensionless hydrodynamic equations are then written as

$$\nabla \cdot \mathbf{u} = 0, \quad (2)$$

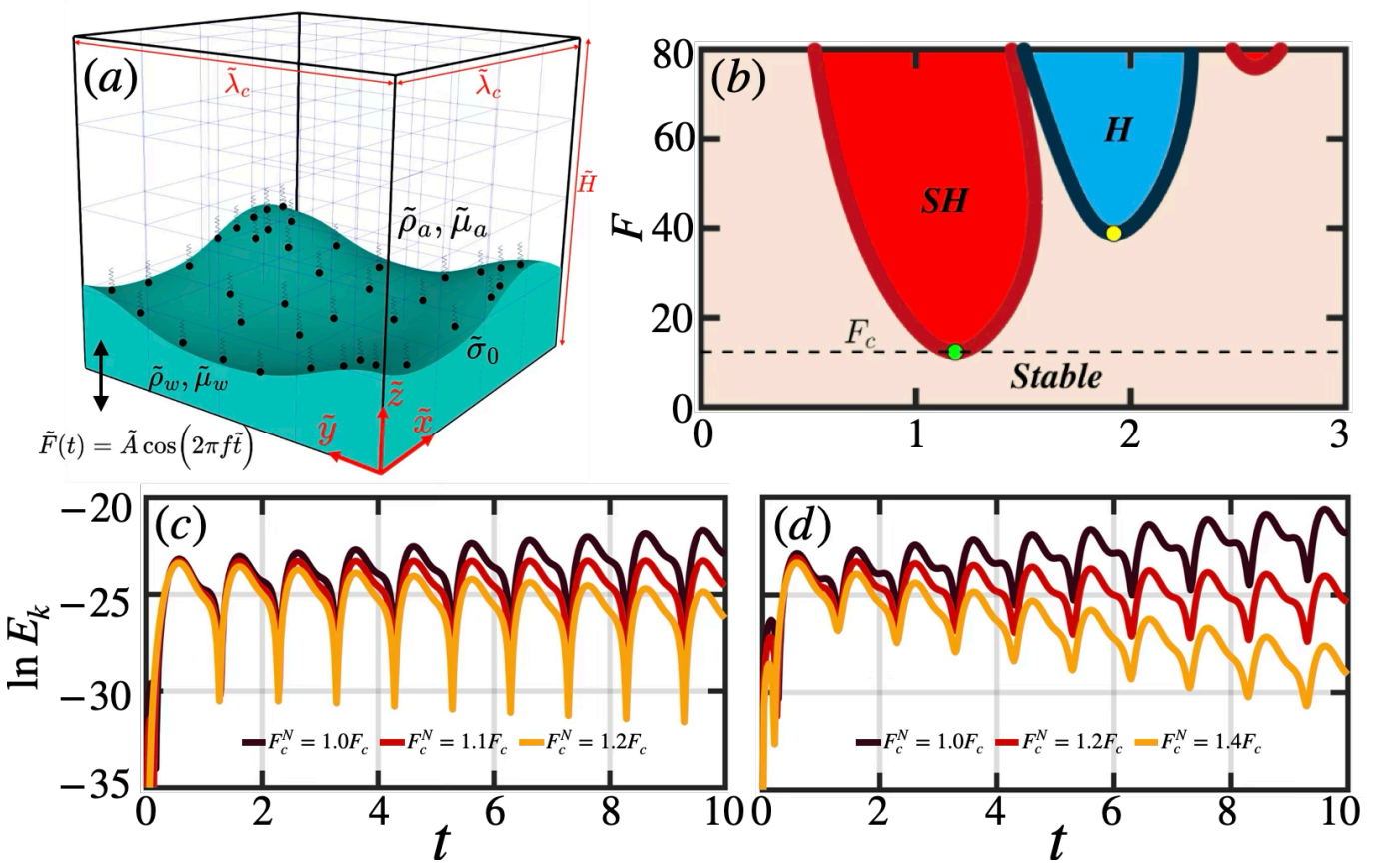


FIG. 1: (a) Schematic representation of the computational domain: the height of the domain $\tilde{H} = 5.00$ mm, and the lateral dimensions $\tilde{\lambda}_c \times \tilde{\lambda}_c$. (b) Critical acceleration F_c for a surfactant-free interface where the solid lines represent the neutral curves for the hydrodynamic parameters listed in [4] and the present work, evaluated using the method of [5]. 'SH' and 'H' refer to the subharmonic and harmonic tongues. (c,d) Temporal evolution of the total kinetic energy E_k for a (c) surfactant-free and (d) surfactant-covered ($\beta_s = 1.0$, $\Gamma_0 = 0.2$) interface at different acceleration amplitudes F . The wavelength in both cases is the critical wavelength $\tilde{\lambda}_c = 5.3023$ mm for the surfactant-free case .

$$\rho \left(\frac{\partial \mathbf{u}}{\partial t} + \mathbf{u} \cdot \nabla \mathbf{u} \right) = -\nabla p - \rho \frac{1}{Fr^2} (1 - F \cos t) \mathbf{i}_z + \frac{1}{Re} \nabla \cdot [\mu (\nabla \mathbf{u} + \nabla \mathbf{u}^T)] + \frac{1}{We} \int_{\mathcal{A}(t)} (\sigma \kappa \mathbf{n} + \nabla_s \sigma) \delta(\mathbf{x} - \mathbf{x}_f) d\mathcal{A}. \quad (3)$$

Here, the dimensionless density and dynamic viscosity are given by

$$\rho = \tilde{\rho}_a / \tilde{\rho}_w + (1 - \tilde{\rho}_a / \tilde{\rho}_w) \mathcal{H}(\tilde{\mathbf{x}}, \tilde{t}), \quad (4)$$

$$\mu = \tilde{\mu}_a / \tilde{\mu}_w + (1 - \tilde{\mu}_a / \tilde{\mu}_w) \mathcal{H}(\tilde{\mathbf{x}}, \tilde{t}). \quad (5)$$

where $\mathcal{H}(\tilde{\mathbf{x}}, \tilde{t})$ is the Heaviside function, which is set to 0 for air (subscript a) and 1 for water (subscript w). The last term on the right-hand-side of (3) corresponds to the surface force at the interface $\mathbf{x} = \mathbf{x}_f$. Inside the integral, the first and second terms account for forces arising from the normal and tangential stresses; the latter are the Marangoni stresses induced by the presence of surface tension gradients. $\mathcal{A}(t)$ refers to the dimensionless time-dependent interfacial area. The dimensionless parameters which appear in (3) are the Reynolds, Weber, Froude number, and the ratio of imposed acceleration \tilde{A} to gravitational acceleration g , given by

$$Re = \frac{\omega \tilde{\rho}_w \tilde{h}^2}{\tilde{\mu}_w}, \quad We = \frac{\omega^2 \tilde{\rho}_w \tilde{h}^3}{\tilde{\sigma}_0}, \quad Fr = \omega \sqrt{\frac{\tilde{h}}{g}}, \quad F = \frac{\tilde{A}}{g}. \quad (6)$$

The interfacial concentration $\tilde{\Gamma}$ evolves according to

$$\frac{\partial \Gamma}{\partial t} + \nabla_s \cdot (\Gamma \mathbf{u}_s) = \frac{1}{Pe} \nabla_s^2 \Gamma, \quad (7)$$

where \mathbf{u}_s is the surface velocity, ∇_s is the gradient in the plane locally tangent to the interface, and Pe is the Peclet number

$$Pe = \frac{\omega \tilde{h}^2}{\mathcal{D}}. \quad (8)$$

The surfactant dynamics are coupled with the hydrodynamics through the nonlinear Langmuir equation of state given by

$$\sigma = \max[0.05, 1 + \beta_s \ln(1 - \Gamma)], \quad (9)$$

where β_s is the surfactant elasticity number:

$$\beta_s \equiv \frac{\mathcal{R} \tilde{\Gamma} \tilde{\Gamma}_\infty}{\tilde{\sigma}_0}, \quad (10)$$

which measures the sensitivity of the surface tension to the surfactant concentration and where the lower limit of σ has been set to 0.05, below which the Langmuir equation of state may diverge. The Marangoni stress τ is a function of Γ :

$$\tau \equiv \nabla_s \sigma \cdot \mathbf{t} = -\frac{\beta_s}{(1 - \Gamma)} \nabla_s \Gamma \cdot \mathbf{t}. \quad (11)$$

In the following section, however, we use a dimensionless parameter B

$$B \equiv \frac{\tilde{\sigma}_0 - \tilde{\sigma}(\tilde{\Gamma}_0)}{\omega \tilde{\mu}_w \tilde{h}} = -\frac{\tilde{\sigma}_0 \beta_s \ln(1 - \tilde{\Gamma}_0 / \tilde{\Gamma}_\infty)}{\omega \tilde{\mu}_w \tilde{h}} \quad (12)$$

to capture the combined effect of β_s and Γ_0 in characterizing the strength of Marangoni stresses.

We refer the readers to [7] for an exhaustive description of the numerical implementation, parallelisation and validation of the numerical framework. Here we briefly summarize the numerical framework: the hybrid level-set/front-tracking method, also known as the Level Contour Reconstruction Method (LCRM) consists of an Eulerian grid on which the single-fluid field equations are solved and an unstructured triangular deforming Lagrangian mesh to track the interface at $\mathbf{x} = \mathbf{x}_f$. The interface is advected by performing a second-order Runge-Kutta integration of $\mathbf{v} = d\mathbf{x}_f/dt$, where \mathbf{v} is the interpolated interfacial velocity obtained via the Eulerian field velocity. Standard cell-centered difference schemes are used for spatial derivatives: the weighted essentially non-oscillatory (WENO) scheme is utilised for the convective terms, the second-order centered difference scheme is implemented for the viscous terms. The second-order Gear method is applied for the temporal discretisation, with implicit time integration for the viscous terms.

B. PROCEDURE, VALIDATION, AND NUMERICAL FINDINGS

We begin by computing the Faraday wave threshold on the surfactant-free (clean) surface using the method for linear stability analysis detailed in [5]. We determined that the critical acceleration amplitude F_c and wavelength λ_c are 12.34 and 5.3023, respectively (see figure 1(b)). We can also compute a threshold from our nonlinear numerical simulations by computing the initial growth rates of the total kinetic energy E_k for several values of F near F_c . Since the growth rate varies linearly with the acceleration near the threshold, we can compute the threshold F_c^N by linear interpolation. For a surfactant-free interface, we considered three acceleration amplitudes $F = (0.9, 1, 1.1)F_c$, as shown in figure 1(b). Interpolation to zero growth rate yields $F_c^N = 12.32$, which differs by only 0.16% from the theoretical F_c , as shown in the first line of table I.

A theoretical linear stability analysis such as that of [5] for a surfactant-covered interface would require linearizing the Langmuir equation of state [8, 9], a task that has not yet been carried out. However, we can compute the acceleration of the numerical threshold $F_c^N(B)$ using the procedure described above. We compute growth rates from numerical simulations with surfactant-covered $\beta_s = 1$ interfaces for different initial surfactant coverage Γ_0 (and corresponding values of B). Although the critical wavelength varies with the elasticity number [9], we approximate it by its surfactant-free value. The resulting thresholds F_c^N are displayed in the next three rows of table I. The same computations were carried out by Ubal et al. [4, 6] using a two-dimensional finite-element technique. Their values are displayed as $F_c^{\text{Ubal}}(B)$ in table I. The relative errors $\delta^{\text{Ubal}} \equiv |F_c^N(B) - F_c^{\text{Ubal}}(B)|/F_c^N$ between our results and those of Ubal et al. are less than 0.7%. The last column of table I shows the strong dependence of the Faraday threshold on the surfactant coverage via the relative increase $\Delta \equiv |F_c^N(B) - F_c|/F_c$.

TABLE I: Numerical threshold acceleration $F_c^N(B)$ for surfactant-free and surfactant-covered interfaces for varying initial surfactant coverage Γ_0 and elasticity number β_s and a fixed wavelength $\lambda_c = 5.3023$. The surfactant-free critical acceleration $F_c = 12.34$ is obtained by using the linear stability method of [5]. The table demonstrates the agreement of our thresholds with those of [4] via $\delta^{\text{Ubal}(B)} \equiv |F_c^N(B) - F^{\text{Ubal}}(B)|/F_c^N(B)$. The last column presents the increase in the Faraday threshold due to surfactant coverage via $\Delta \equiv (F_c^N(B) - F_c(0))/F_c(0)$.

β_s	Γ_0	B	Present work (F_c^N)	F^{Ubal} [4]	δ^{Ubal} (%)	Δ (%)
clean	0	0	12.32	12.30	0.16	0.16
1.0	0.1	0.44	13.09	13.00	0.69	6.07
1.0	0.2	0.89	15.45	15.50	0.32	25.2
1.0	0.3	1.33	18.47	18.51	0.21	49.7

TABLE II: Numerical threshold acceleration F_c^N for wavelength $\lambda_c = 5.3023$ and varying β_s , Γ_0 , and B , and its relative increase $\Delta \equiv (F_c^N - F_c)/F_c$ from surfactant-free case, for which $F_c = 12.34$ [5]. The highlighted data is used in fig. 1 in the main text.

β_s	Γ_0	B	F_c^N	Δ (%)
0.10	0.50	0.30	13.02	5.51
0.85	0.10	0.40	13.09	6.07
0.25	0.40	0.57	14.69	19.0
0.15	0.60	0.61	15.32	24.1
0.20	0.50	0.62	15.45	25.2
0.65	0.20	0.65	15.62	26.5
0.75	0.20	0.75	15.92	29.0
0.50	0.30	0.79	16.05	30.0
0.35	0.40	0.80	16.09	30.4
0.30	0.50	0.92	16.45	33.4
0.45	0.40	1.02	17.65	43.0
0.80	0.25	1.03	17.72	43.6
0.35	0.50	1.08	18.58	50.5
0.50	0.40	1.14	18.61	50.8
0.40	0.50	1.23	18.63	51.0
0.60	0.40	1.37	18.92	53.3
0.45	0.50	1.39	19.01	54.0
0.35	0.60	1.42	19.08	54.6
0.50	0.50	1.51	19.18	55.4
0.45	0.60	1.83	20.08	62.7
0.60	0.50	1.85	20.83	68.8
0.70	0.50	2.16	20.99	70.0

Table II shows the increase in the Faraday threshold for many other values of elasticity number β_s and surfactant coverage Γ_0 . The damping rate increases with either of these parameters, leading to an increase in the threshold of Faraday waves. We note that the threshold depends almost entirely on their combination, B ; that is, when β_s and Γ are varied so as to produce the same value of B , then F_c^N is unchanged. See, for example, the parameter pairs $(\beta_s = 0.45, \Gamma_0 = 0.40)$, which yields $B = 1.02$ $F_c^N = 43.0$ and $(\beta_s = 0.80, \Gamma_0 = 0.25)$, which yield $B = 1.03$ and $F_c^N = 43.6$. Other pairs of (β, Γ_0) values that yield very close values of B and F_c^N can also be seen in table II.

* o.matar@imperial.ac.uk

- [1] N. Périnet, D. Juric, and L. S. Tuckerman, Numerical simulation of Faraday waves, *J. Fluid Mech.* **635**, 1 (2009).
[2] L. Kahouadji, N. Périnet, L. S. Tuckerman, S. Shin, J. Chergui, and D. Juric, Numerical simulation of supersquare patterns in Faraday waves, *J. Fluid Mech.* **772**, R2 (2015).
[3] L. Kahouadji, D. Panda, L. Tuckerman, S. Shin, J. Chergui, D. Juric, and O. Matar, Poster: Faraday uncaged, in *76th Annual Meeting of the APS Division of Fluid Dynamics* (American Physical Society, 2023).
[4] S. Ubal, M. D. Giavedoni, and F. A. Saita, The formation of Faraday waves on a liquid covered with an insoluble surfactant: Influence of the surface equation of state, *Lat. Am. Appl. Res.* **35**, 59 (2005).

- [5] K. Kumar and L. S. Tuckerman, Parametric instability of the interface between two fluids, *J. Fluid Mech.* **279**, 49 (1994).
- [6] S. Ubal, M. D. Giavedoni, and F. A. Saita, Elastic effects of an insoluble surfactant on the onset of two-dimensional Faraday waves: a numerical experiment, *J. Fluid Mech.* **524**, 305 (2005).
- [7] S. Shin, J. Chergui, and D. Juric, A solver for massively parallel direct numerical simulation of three-dimensional multiphase flows, *J. Mech. Sci. Tech.* **31**, 1739 (2017).
- [8] S. Kumar and O. K. Matar, Parametrically driven surface waves in surfactant-covered liquids, *Proc. Roy. Soc. A* **458**, 2815 (2002).
- [9] S. Kumar and O. K. Matar, On the Faraday instability in a surfactant-covered liquid, *Phys. Fluids* **16**, 39 (2004).